iopscience.iop.org

Home Search Collections Journals About Contact us My IOPscience

Combination of principal component analysis and optical-flow motion compensation for improved cardiac MR thermometry

This content has been downloaded from IOPscience. Please scroll down to see the full text.

2017 Phys. Med. Biol. 62 1208

(http://iopscience.iop.org/0031-9155/62/4/1208)

View the table of contents for this issue, or go to the journal homepage for more

Download details:

IP Address: 193.54.215.193
This content was downloaded on 24/01/2017 at 15:59

Please note that terms and conditions apply.

You may also be interested in:

An improved optical flow tracking technique for real-time MR-guided beam therapies in moving organs
C Zachiu, N Papadakis, M Ries et al.

Referenceless MR thermometry—a comparison of five methods
Chao Zou, Changjun Tie, Min Pan et al.

Image-driven, model-based 3D abdominal motion estimation for MR-guided radiotherapy
Bjorn Stemkens, Rob H N Tijssen, Baudouin Denis de Senneville et al.

Performance analysis of a dedicated breast MR-HIFU system for tumor ablation in breast cancer patients
R Deckers, L G Merckel, B Denis de Senneville et al.

Ultrasonography-based 2D motion-compensated HIFU sonication integrated with reference-free MR temperature monitoring: a feasibility study ex vivo
Vincent Auboiroux, Lorena Petrusca, Magalie Viallon et al.

Fast generation of 4D PET-MR data from real dynamic MR acquisitions
C Tsoumpas, C Buerger, A P King et al.

Dynamic frame selection for in vivo ultrasound temperature estimation during radiofrequency ablation
Matthew J Daniels and Tomy Varghese

Multi-gradient echo MR thermometry for monitoring of the near-field area during MR-guided high intensity focused ultrasound heating
Mie K Lam, Martijn de Greef, Job G Bouwman et al.

IOP Publishing | Institute of Physics and Engineering in Medicine Physics in Medicine & Biology
Phys. Med. Biol. **62** (2017) 1208–1224 doi:10.1088/1361-6560/aa51f9

Combination of principal component analysis and optical-flow motion compensation for improved cardiac MR thermometry

S Toupin[1,2,3], B Denis de Senneville[4], V Ozenne[1,2], P Bour[1,2,5], M Lepetit-Coiffe[3], M Boissenin[1,2], P Jais[1,2,6] and B Quesson[1,2]

[1] IHU Liryc, Electrophysiology and Heart Modeling Institute, Foundation Bordeaux University, F-33600 Pessac-Bordeaux, France
[2] INSERM, Centre de recherche Cardio-Thoracique de Bordeaux, U1045, F-33000 Bordeaux, France
[3] Siemens Healthineers France, F-93210 Saint-Denis, France
[4] Institute of Mathematics of Bordeaux, UMR 5251, F-33400 Talence, France
[5] Image Guided Therapy, F-33600 Pessac, France
[6] Bordeaux University Hospital (CHU), Electrophysiology and Ablation Unit, F-33600 Pessac, France

E-mail: solenn.toupin@ihu-liryc.fr

Received 13 September 2016, revised 24 November 2016
Accepted for publication 6 December 2016
Published 23 January 2017

Abstract

The use of magnetic resonance (MR) thermometry for the monitoring of thermal ablation is rapidly expanding. However, this technique remains challenging for the monitoring of the treatment of cardiac arrhythmia by radiofrequency ablation due to the heart displacement with respiration and contraction. Recent studies have addressed this problem by compensating in-plane motion in real-time with optical-flow based tracking technique. However, these algorithms are sensitive to local variation of signal intensity on magnitude images associated with tissue heating. In this study, an optical-flow algorithm was combined with a principal component analysis method to reduce the impact of such effects. The proposed method was integrated to a fully automatic cardiac MR thermometry pipeline, compatible with a future clinical workflow. It was evaluated on nine healthy volunteers under free breathing conditions, on a phantom and *in vivo* on the left ventricle of a sheep. The results showed that local intensity changes in magnitude images had lower impact on motion estimation with the proposed method. Using this strategy, the temperature mapping accuracy was significantly improved.

Keywords: MR thermometry, cardiac MRI, motion estimation, principal component analysis

(Some figures may appear in colour only in the online journal)

1. Introduction

Catheter-based radiofrequency (RF) ablation has become a reference therapy to treat cardiac arrhythmia. Abnormal electrical pathways that trigger for unwanted cardiac contractions can be isolated from the healthy myocardium by creating a local thermal lesion surrounding the pathologic region. RF energy is delivered through an electrode located at the tip of a catheter advanced into the heart. However, the risk of arrhythmia recurrence remains significant (Tanner *et al* 2010, Weerasooriya *et al* 2011), mainly due to incomplete isolation of circuit or by recovery of previously isolated circuit. Hence, one major challenge of RF ablation is the ability to create permanent and transmural lesions to ensure the efficacy and the safety of the procedure. The success rate of the therapy may be improved by directly monitoring the myocardial necrosis formation to predict the size of the final tissue injury (Wittkampf and Nakagawa 2006). Catheter orientation, blood flow in the cardiac cavities and catheter/tissue contact are the main factors that significantly influence the lesion size. Because of the variability of these factors *in vivo*, energy and duration of the RF delivery can hardly predict the therapy outcome. Since the electrode temperature does not reflect the temperature of the tissue at distance of the contact point, surrogate measures have been proposed such as changes of circuit impedance, electrogram amplitude and catheter/tissue contact force. These techniques were found to help to prevent excessive heating and associated complications (perforation, thrombus, atrioesophagial fistulas…). However, none of them correlated with tissue temperature and final lesion size.

Magnetic resonance (MR) thermometry, using the water proton resonance frequency (PRF) shift technique, is a non-invasive technique to measure the temperature distribution in tissue. This method has been of growing interest in recent years for the monitoring of thermal ablation in various organs such as liver (Seror *et al* 2008, Holbrook *et al* 2010), prostate (Ramsay *et al* 2013), uterus (McDannold *et al* 2006) and brain (de Senneville *et al* 2007, Lipsman *et al* 2013). However, cardiac MR thermometry remains very challenging because of complex organ motion resulting from heart contraction and respiratory motion. The three following hurdles must be overcome. (1) MR acquisition must be fast enough to avoid intra-scan motion, resulting in blurring and ghosting artifacts. (2) All images in the time series must be registered at an identical position, to allow the reliable calculation of temperature and cumulative thermal dose (Sapareto and Dewey 1989), based on the temporal integration of the temperature on a pixel-by-pixel basis. (3) Change in lung volume during the breathing cycle modifies the local magnetic field in the heart and induces additional periodic variations on phase images in the heart. Since the PRF thermometry method is based on the linearity between the temperature variations and the phase changes, these effects cause significant artifacts that can bias the temperature measurements.

To overcome these issues, several techniques have been proposed in the past. (1) Fast imaging, such as single-shot echo planar imaging (EPI), was combined with electrocardiogram (ECG) triggering to allow the acquisition of several slices per heartbeat with limited intra-scan motion and heart contraction motion (de Senneville *et al* 2012, Ozenne *et al* 2016). (2) All magnitude and phase images in the time series are registered accordingly to a selected reference data. Since temperature information is encoded into the phase image, magnitude image can be used to estimate and compensate organ displacement between consecutive images using optical-flow algorithm. (3) To correct for susceptibility artifacts, a number of MR images are usually acquired before starting the thermal ablation (learning step) to create a set of reference data that can be used to remove susceptibility related phase variations (Roujol *et al* 2010). Using such a strategy, cardiac MR thermometry was recently reported with a spatial resolution of $1.6 \times 1.6 \times 3\,\text{mm}^3$ and an imaging time of ~100 ms per slice (Ozenne *et al* 2016).

In this previous study, an optical-flow algorithm (Horn and Schunck 1981) was used to compute vector fields representing displacement between each new magnitude image and the image at a reference position. This algorithm requires the calibration of only one parameter and ensures a fast convergence which is advantageous for applications with real-time processing requirements. However, it relies on the assumption of conservation of local intensity that can be violated during RF ablation due to changes in tissue properties with heating (Graham *et al* 1998). MR relaxation times, such as T1, T2 and $T2^*$, can indeed vary with temperature and tissue may also change when a thermal lesion is created (e.g. edema). These effects can result in local intensity variations on the magnitude images, also depending on the MR acquisition pulse sequence. As a result, these local intensity changes may be interpreted as motion and lead to local erroneous displacement vector field. Since this motion field is used to register the phase images used by the PRF method, the MR thermometry precision may thus be compromised as well.

To overcome potential issues of the Horn and Schunck (H&S) optical-flow algorithm in the context of MR thermometry, a new technique has recently been proposed (Denis de Senneville *et al* 2015). The method consists in applying conventional H&S algorithm over the data collected during the learning step before ablation, since no intensity variation is expected. Then, a principal component analysis (PCA) is performed over the resulting motion field vectors to extract eigenvectors and eigenvalues that are related to motion. During thermal ablation, the motion is estimated from each new magnitude image as a linear combination of these eigenvectors, making the method less sensitive to potential variations of intensity when tissue temperature is locally changing.

This present work focuses on the evaluation of this optical-flow based method associated with PCA, called PCA-based H&S, in the context of cardiac MR thermometry during RF ablation. The performance of the method was evaluated on simulated intensity variations on magnitude images, on experimental data obtained on a static/mobile phantom during RF ablation, on experimental images from 9 healthy volunteers under free breathing conditions without heating and during cardiac RF ablation performed *in vivo* on the left ventricle (LV) of a sheep.

2. Material and methods

2.1. MR Thermometry imaging protocol

Dynamic MR thermometry was performed at 1.5 T (Avanto, Siemens Healthcare, Germany) using two standard 16-channel cardiac coils. A fat-saturated, single-shot EPI pulse sequence was combined with GRAPPA (acceleration factor of 2) to achieve a spatial resolution of $1.6 \times 1.6 \times 3\,\text{mm}^3$, TE/TR/flip angle (FA) = 18–20 ms/110 ms/60°, bandwidth = 1576 Hz/pixel, field of view (FoV) = $180 \times 180\,\text{mm}^2$. Through-plane motion was minimized by setting the imaging slices parallel to the principal respiration direction (head-feet). Saturation slabs were positioned along the FoV in the phase encoding direction to avoid aliasing. Acquired EPI raw data were streamed online via TCP/IP to a remote computer for image reconstruction (Hansen and Sørensen 2013) and for real-time computation of temperature maps.

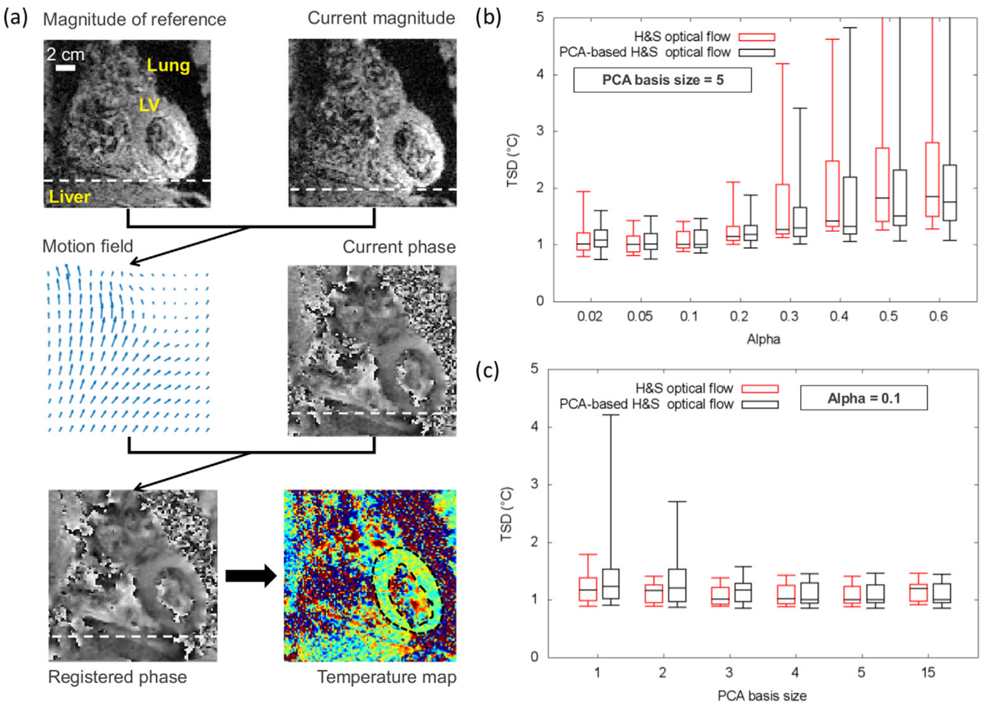

Figure 1. Calibration of Horn and Schunck (H&S) and PCA-based H&S optical-flow algorithms. (a) The motion is estimated between each current magnitude image and a magnitude image of reference using either H&S or PCA-based H&S optical-flow algorithms. The resulting motion field is used to register the current phase image. Finally the final temperature map is calculated from the registered phase using the PRF method. Calibration is computed depending on the regularization term α (b) and the size of PCA basis (c), i.e. the number of eigenvectors used in the PCA algorithm. Performance of algorithms is evaluated in terms of MR thermometry accuracy, given by the standard deviation of the temperature evolution in time (TSD). Different values of α and number of eigenvectors were tested for both algorithms over all volunteers ($N = 9$). For each graph, the thresholds correspond to 5% (lower horizontal bar), 25% (lower limit of the box), median value (horizontal line inside the box), 75% (upper limit of the box) and 95% (upper horizontal bar) of the distribution of TSD in pixels included in the ROI surrounding the LV (delineated by the black dashed line on temperature map in (a)), pooled together from data from all volunteers.

2.2. Image registration

For each image in the time series, displacement field (u,v) was estimated from magnitude images (see figure 1(a)) and used to register both magnitude and phase images at a fixed position (the first image in the time series was taken as the reference position). Conventional H&S optical-flow algorithm is based on the minimization of the energy E (1).

$$E(u,v) = \int_{x,y} \left(I_x u + I_y v + I_t\right)^2 + \alpha\left(\|\nabla u\|_2^2 + \|\nabla v\|_2^2\right) \mathrm{d}x\mathrm{d}y \tag{1}$$

Where x and y are the pixel coordinates, u and v the horizontal and vertical displacement vector components, $I_{x,y,t}$ the spatio-temporal partial derivatives of the magnitude intensity and α

a tunable weighting factor. Since this method relies on the local conservation of the intensity, the drop in signal intensity induced by heating and changes in tissue properties may introduce errors in the estimated motion (u, v).

The PCA-based H&S method requires a preparative learning step which covers several breathing cycles before the ablative procedure (typically 20 frames). 2D estimated motion fields (u, v) together with registered phase images are collected using the conventional H&S method (1) since local variations of intensity are unexpected. Then a PCA is performed on the motion fields of the learning step:

$$\begin{pmatrix} u(x,y) \\ v(x,y) \end{pmatrix} = \sum_{k=1}^{M} d_k \begin{pmatrix} \Phi_k(x,y) \\ \Psi_k(x,y) \end{pmatrix} \tag{2}$$

Where $\Phi_{k=1\ldots M}$ and $\Psi_{k=1\ldots M}$ are the horizontal and vertical components of the eigenvector $\#k$, $d_{k=1\ldots M}$ are the eigenvalues representing motion descriptors and M is the number of eigenvectors.

During the interventional procedure, for each new incoming image, the 2D motion is estimated as a linear combination of the previously calculated eigenvectors. For that purpose, the following PCA-based H&S equation (3) is minimized:

$$\begin{aligned} E\left(\sum_{k=1}^{M} d_k \Phi_k(x,y), \sum_{k=1}^{M} d_k \Psi_k(x,y)\right) = \int_{x,y} \left(I_x \sum_{k=1}^{M} d_k \Phi_k(x,y) + I_y \sum_{k=1}^{M} d_k \Psi_k(x,y) + I_t\right)^2 \\ + \alpha \left(\left\| \nabla \sum_{k=1}^{M} d_k \Phi_k(x,y) \right\|_2^2 + \left\| \nabla \sum_{k=1}^{M} d_k \Psi_k(x,y) \right\|_2^2 \right) \mathrm{d}x\mathrm{d}y \end{aligned} \tag{3}$$

The minimization of the functional E was described in Denis de Senneville *et al* (2015) and provided in the RealTITracker[7] free toolbox. Conventional H&S and PCA-based H&S methods were both used to register magnitude/phase images in order to evaluate the impact of the algorithms on MR thermometry performance. To improve the estimation of large displacements, a coarse-to-fine multi-resolution scheme was performed with three levels up to the original image resolution (112 × 112 pixels). To ensure the convergence of the optical-flow algorithms, $(\sqrt{u^2 + v^2})$ was averaged over all the pixels of the image between two successive iterations and compared to a convergence criteria given by $\left(\frac{0.1}{l+1}\right)$, where l is the level of the multi-resolution scheme. At the last level of the pyramid, where the image size is maximal, l value is 0 and the convergence criteria value is 0.1.

The weighting factor α regulates the link between intensity variation and motion field regularity and must be experimentally determined to optimize the robustness of the motion estimation on representative MR images. Values of α range between 0 and 1 and large values lead to a smoother flow. The number of eigenvectors used in the PCA basis can influence the robustness of the motion estimation as well. The first eigenvector represents the main contribution of the motion, while the eigenvectors associated with lower eigenvalues encode for local deformations and for the noise.

The optical-flow algorithms were implemented in C++ and evaluated on a Core i7-4790 processor (3.6 GHz, four cores, INTEL, Santa Clara, CA, USA) without GPU implementation.

---

[7] http://bsenneville.free.fr/RealTITracker

2.3. Thermometry mapping

The PRF thermometry method computes temperature change ΔT from difference between a given phase image φ_t acquired during treatment and a reference phase image φ_{ref} acquired prior to heating (4).

$$\Delta T = (\varphi_t - \varphi_{\text{ref}}) \cdot k \qquad \text{with}\, k = (\gamma \cdot \sigma \cdot B_0 \cdot \text{TE})^{-1} \tag{4}$$

Where γ is the gyromagnetic ratio (≈42.58 MHz T^{-1}), $\sigma = -0.0094\,\text{ppm} \cdot {}^{\circ}\text{C}^{-1}$ is the PRF temperature coefficient, B_0 is the magnetic field strength (=1.5 T) and TE is the echo time. The registered phase images of the learning step were used to build a parameterized flow model using a PCA algorithm on a pixel-by-pixel basis. During the intervention, the background phase φ_{ref} is computed with the learned model and subtracted to the current registered phase image φ_t. Details on this method can be found in Roujol *et al* (2010). Temperature maps computation was followed by temporal temperature filtering using a low-pass Butterworth filter (first order, cutoff frequency of 0.14 Hz), as described in Ozenne *et al* (2016).

2.4. Volunteer study

Thermometry performance was evaluated with both algorithms by computing the temporal standard deviation of the temperature (TSD) in each pixel over a 2–3 min acquisition (250 successive acquisitions triggered on the cardiac cycle). A region of interest (ROI) surrounding the LV was manually drawn to select pixels included in the analysis. The regularization term α and the number of PCA eigenvectors M were experimentally determined from the analysis of temperature data acquired on nine volunteers under free-breathing conditions. Performances of the algorithms were then compared with the same value of α and size of PCA basis. The significance between the TSD obtained with H&S and PCA-based H&S optical-flow methods was evaluated using a *t*-test with a significance level of 1%. Each pixel of the ROI surrounding the LV was included in the statistical analysis.

2.5. Phantom study

2.5.1. Simulation of intensity variation on MR images of an agar phantom. A first study was performed on a home-made cylindrical tissue-mimicking phantom (3% dry-weight agar) as described in Rickey *et al* (1995). To evaluate the robustness of PCA-based H&S algorithm in the case of local variation of intensity on magnitude images, several patterns of signal decrease were added to the magnitude image of the phantom into which a catheter was inserted. A Gaussian function of amplitude A (expressed in percent of the maximal image intensity from native experimental images) and variance μ was computed and subtracted to the original magnitude image to mimic the impact of a typical RF lesion. The resulting bias in image registration was computed for different values of A (ranging from 10% to 100%) and μ (ranging from 0.5 to 2.9 pixels) by calculating the average and the maximal endpoint error (EE) (5) over a ROI of 9 × 9 pixels centered on simulated area.

$$EE = \sqrt{(u - u_{\text{ref}})^2 + (v - v_{\text{ref}})^2} \tag{5}$$

Where (u, v) and $(u_{\text{ref}}, v_{\text{ref}})$ are the estimated and the reference motion, respectively. $(u_{\text{ref}}, v_{\text{ref}})$ is the motion estimated on the original image and is considered as the gold standard motion while (u, v) is the motion estimated on the modified image including simulated signal change. EE maps were computed individually with the PCA-based H&S and the conventional H&S

optical-flow methods for comparison of the robustness of the proposed method with the original one.

2.5.2. Experimental validation on a gel phantom.

A RF ablation was run at 10 W for 60 s with simultaneous temperature mapping on the phantom without motion. A MR compatible catheter (Biosense Webster, Diamond Bar, CA) inserted into the gel was connected to a clinical RF generator (Stockert Medical Solution, Freiburg, Germany) located outside the Faraday cage. An optical probe (Luxtron probe, LumaSense technologies, Santa Clara, CA) was positioned close to the catheter tip to measure the absolute temperature evolution.

The gold standard temperature map ΔT_{ref} is first calculated by simple phase subtraction (4) without image registration, since the phantom is static. Then, temperature maps were calculated after image registration using H&S and PCA-based H&S optical-flow methods. The potential artifact, introduced by the motion correction due to signal intensity variation on magnitude images, was quantified by calculating the motion fields EE (5) and the temperature errors δT (6) relative to reference temperature data ΔT_{ref}, for each method:

$$\delta T = \frac{1}{N}\sum_{t=1}^{N}\left|\Delta T(t) - \Delta T_{\text{ref}}(t)\right| \tag{6}$$

where ΔT is the temperature elevation measured with an optical-flow based motion estimation, ΔT_{ref} is the reference temperature increase computed without motion compensation and N is the number of dynamic acquisitions in the time series.

After a cooling period was observed, an identical RF ablation was performed while the phantom underwent a periodic motion (15 cycles min^{-1}) of ~8 mm amplitude along z axis of the magnet using an inflated balloon strapped to the phantom and driven by a MR compatible ventilator (Aestivia, General Electric, Fairfield, CT). Temperature maps were computed and compared for the two different methods of motion estimation and correction. The calculation of the gold standard temperature ΔT_{ref} was not possible because of the phantom movement.

2.6. In vivo ablation in the LV of a sheep

Animal experiment was conducted *in vivo* on a sheep after approval of the protocol by the ethic committee of the University of Bordeaux. Identical MR compatible catheter was advanced into the LV under fluoroscopy (Toshiba InfiniX, Toshiba Medical, Nasu, Japan). The animal was then installed in a supine position in the MRI scanner and maintained under controlled respiration (15 cycles min^{-1}). Cardiac triggered MR temperature images were acquired prior and during a RF ablation at 30 W for 60 s.

2.6.1. Simulation of intensity variation on MR images of a sheep heart.

As a first test, local intensity variations were added in the vicinity of the catheter tip on one magnitude image of the time series without heating, using identical methodology as on agar gel phantom. The resulting bias was quantified by calculating the average and the maximal EE (5) over a ROI of 9×9 pixels centered on the simulated area.

2.6.2. Experimental validation in the LV of a sheep.

MR images acquired during RF ablation were computed in post-processing using the two different motion estimation algorithms and resulting temperature images were compared.

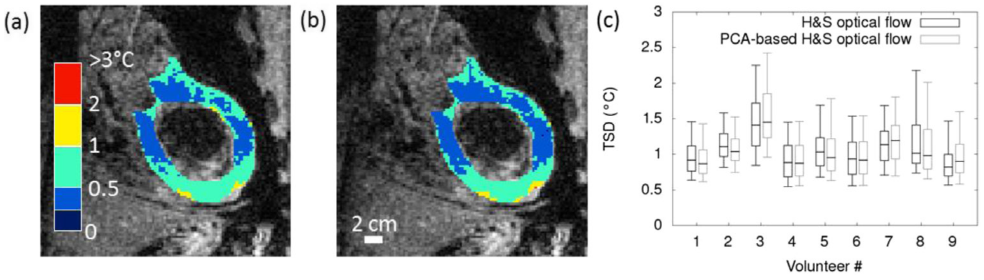

Figure 2. Temperature standard deviation (TSD) for both optical-flow methods applied to MR temperature images from free-breathing volunteers. The TSD is computed on a pixel-by-pixel basis over the 2–3 min of dynamic acquisition. TSD is compared when H&S and PCA-based H&S methods are employed for in-plane motion registration. Typical results obtained on the LV of a healthy volunteer (colored pixels, volunteer #5) are displayed in (a) H&S and (b) PCA-based H&S. Both methods were tested with a weighting factor $\alpha = 0.1$, a number of eigenvectors of 5 and identical temperature mapping data processing. Boxplots (c) relate the distribution of TSD in a ROI surrounding the LV for images from the nine tested volunteers.

3. Results

3.1. Volunteer study

The displacement of the LV induced by respiratory motion was 8.3 ± 0.3 mm on average in the nine volunteers. Figure 1 depicts the calibration of H&S and PCA-based H&S optical-flow algorithms over all data-sets. Regularization term $\alpha = 0.1$ was found to minimize the TSD (figure 1(b)), whereas TSD distribution remained similar when the number of eigenvectors was larger than two (figure 1(c)). For all data obtained on volunteers, the number of eigenvectors was set to 5, which represented more than 99% of the total energy (sum of the eigenvalues).

Figure 2 compares the performances of conventional H&S and PCA-based H&S algorithms on MR temperature images from all volunteers. TSD maps obtained on volunteer #5 are reported with the conventional H&S optical-flow approach (figure 2(a)) and with the proposed PCA-based H&S method (figure 2(b)). Over all volunteers, the temperature stability remained similar for both motion correction strategies, with averaged TSD over the pixels of the LV ROI of 1.06 ± 0.35 °C (H&S) and 1.05 ± 0.40 °C (PCA-based H&S), respectively. The *t*-test showed a statistically non-significant difference between the two methods ($p > 0.01$).

3.2. Phantom study

Figure 3 shows EE of flow fields computed on simulated signal variations around a catheter tip inserted in the static phantom (figure 3(a)), without heating. Examples of simulated patterns with $A = 80\%$ of maximal signal decrease are shown in figure 3(b) and applied to the MR images of the gel in figure 3(c). The conventional H&S optical-flow displayed higher EE than PCA-based H&S. With a signal decrease A of 80%, the maximal EE was in the range of 1.1–3.5 mm with H&S (figure 3(d)) and of 0.03–0.2 mm with PCA-based H&S (figure 3(e)), for values of μ ranging from 0.9 to 2.9 pixels. As shown on contour plots, EE increased with the amplitude A and the variance μ of the simulated signal drop. On average on the 9×9 pixels ROI, the mean EE value increased up to 2 mm with H&S method, whereas it remained around 0.1 mm with the PCA-based method.

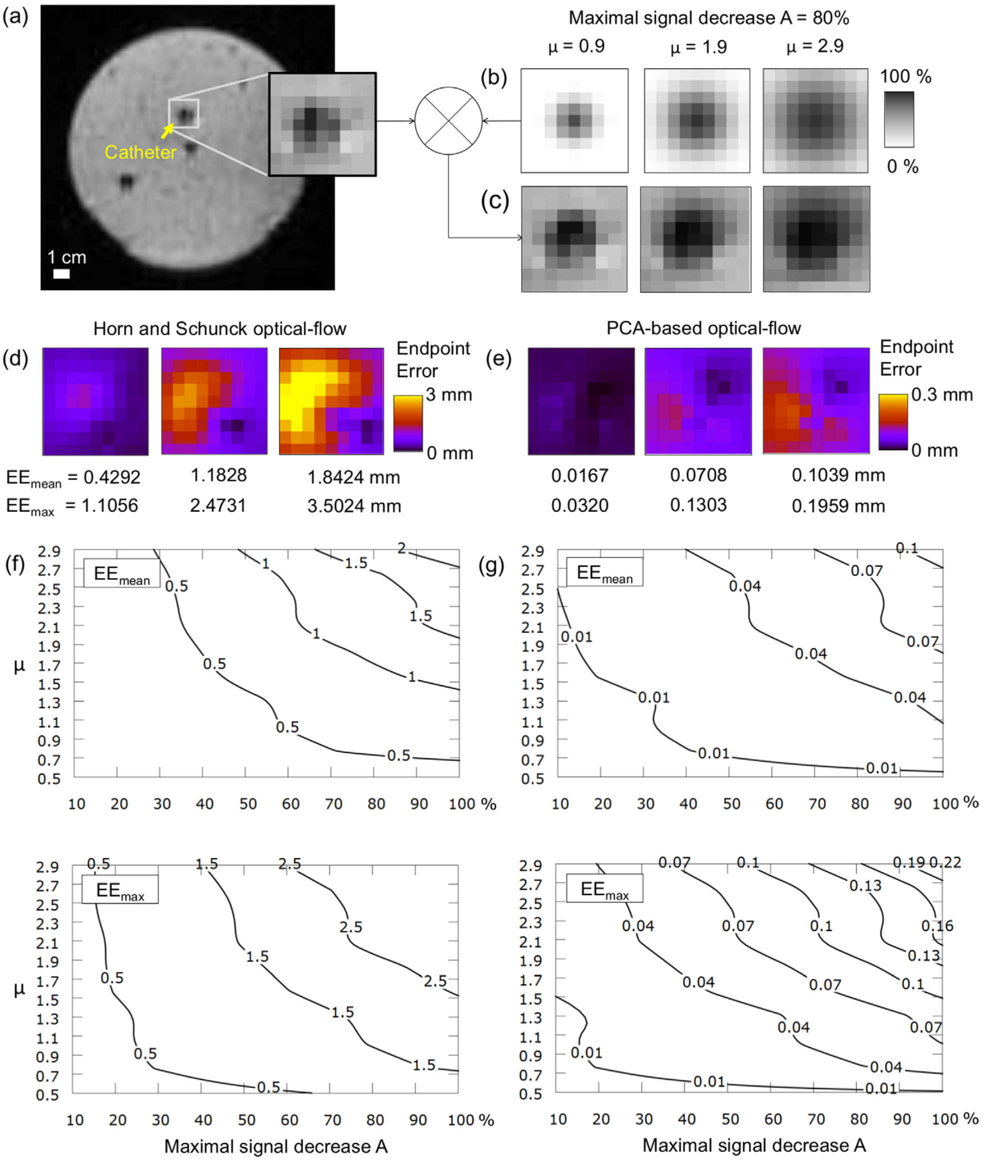

Figure 3. Simulation of a local signal decrease on the magnitude image of an agar gel phantom (a) centered on the catheter position. The imaging plane was positioned perpendicular to the catheter, near the tip. Several patterns of signal drop were computed depending on the variance μ in pixels and the maximal decrease A in percentage. Example of patterns is shown in (b) with 80% of signal loss in the central pixel of the ROI (9×9 pixels). Motion estimation was performed on the resulting simulated magnitude images (c). The motion fields endpoint error (EE) was computed in millimeters (1 pixel = 1.6 mm) with H&S (d) and PCA-based H&S (e) optical-flow methods. Average and maximal values over the ROI are annotated below. Averaged and maximal EE were calculated for each pattern and summed up on contour plots (f) H&S and (g) PCA-based H&S.

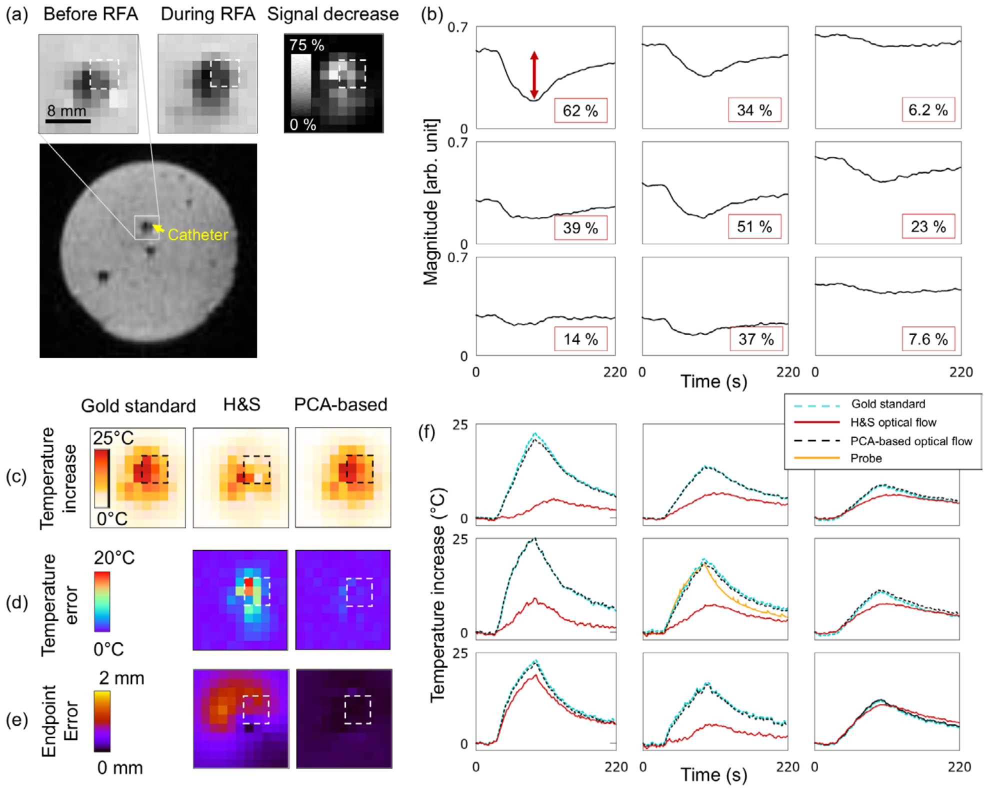

Figure 4. Experimental data obtained on a static agar gel phantom. A RF ablation was run for 60 s at 10 W using a MR compatible catheter inserted in agar gel (a). A decrease of the magnitude signal was observed during the RF ablation. The pixels corresponding to the white dashed box are plotted in (b). (c) Temperature elevation calculated with H&S optical-flow and with PCA-based optical-flow algorithm was compared with temperature measured without any motion correction (Gold standard). Bias introduced by motion registration was evaluated in terms of temperature error (d) and motion fields EE in millimeters (1 pixel = 1.6 mm) (e). Evolution of temperature (f) in time in pixels of a ROI of 3 × 3 pixels (dashed box) was plotted. The curve resulting from optical fiber temperature probe measurements is plotted in the central pixel which corresponds to the closest location of the probe.

The impact of flow field errors on temperature measurement was measured by performing a RF ablation at 10 W for 60 s. The magnitude decrease during the ablation is illustrated by performing the difference between two images, before and during the ablation (figure 4(a)). Evolution of magnitude in time in 3 × 3 pixels is described in figure 4(b) and is correlated with the phantom properties changes during the heating. Temperature maps measured with each method were compared to gold standard temperature map, computed without motion correction (figure 4(c)). Heating zone was highly distorted by the errors of the flow field estimated with H&S optical-flow, with a temperature error up to 15 °C (figure 4(d)) due to an EE in motion estimation of 1.5 mm (figure 4(e)). Maximal intensity decrease was about 60% and the thickness of the spot was equivalent to $\mu = 1.3$ pixels. EE was thus in agreement with simulation results displayed in figure 3. In contrast, using the PCA-based method, the EE was found below 0.05 mm and the temperature error below 1.5 °C. Temperature evolution in time

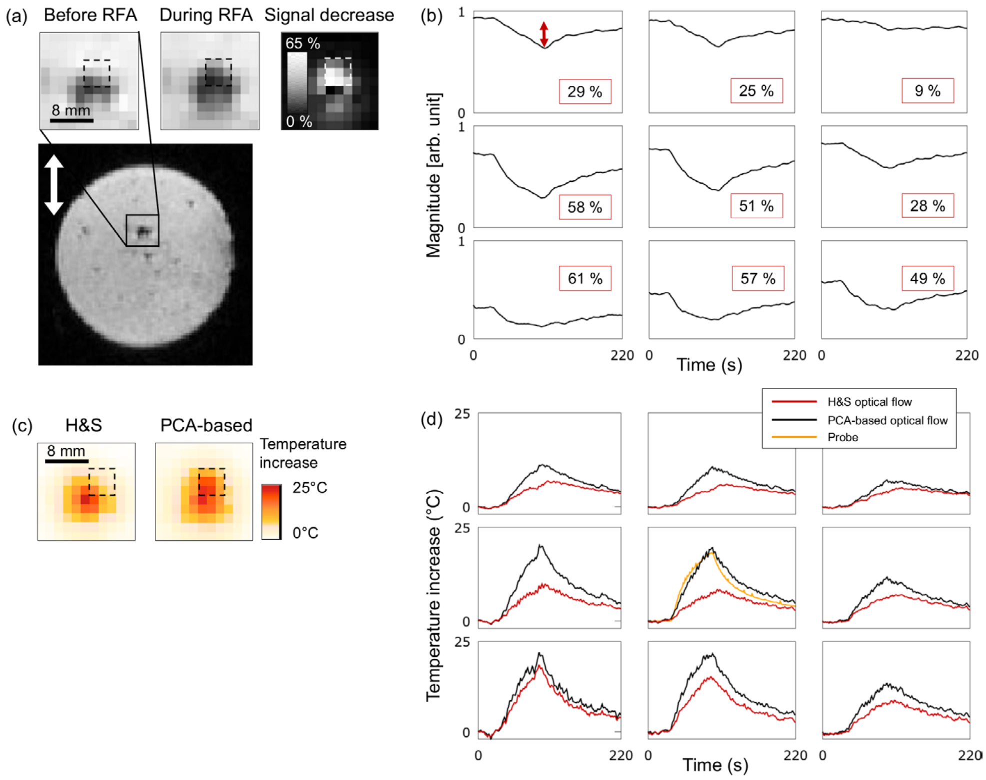

Figure 5. Experimental data obtained on an agar gel phantom. A RF ablation (10 W for 60 s) was run on a mobile phantom (translation induced by a mechanical ventilator) and monitored by MR thermometry. Heating induced local intensity variation around the catheter tip (a). Signal loss in 3 × 3 pixels of a ROI (dashed box) is plotted in (b). (c) Temperature map at the end of the RF delivery using H&S and PCA-based H&S algorithms in a 11 × 11 pixels area centered on the catheter tip. (d) Temperature evolution in time on pixels of the dashed black boxes, centered on optical probe location.

in a ROI of 3 × 3 pixels was plotted in figure 4(f) and illustrated the bias introduced by each tested methods.

During RF ablation on the gel and in presence of motion (figure 5), similar drop in signal intensities near the catheter tip was observed (figures 5(a) and (b)), with a maximal decrease of 60% and a variance of 1.1 pixel. Temperature maps computed with the conventional H&S method showed an underestimation of up to 15 °C (figures 5(c) and (d)) while temperature from the PCA-based H&S algorithm followed readings from the temperature probe (see central plot in figure 5(d)). The presence of motion affected slightly the temperature accuracy (additional noise in temperature signals) despite the use of optical-flow motion registration and susceptibility artifact correction algorithm. However, obtained temperature measurements were similar to those computed on a phantom without motion. Note that the presence of motion prevents the calculation of the gold standard temperature by simple phase subtraction.

3.3. In vivo ablation in the LV of a sheep

Figure 6(a) shows one magnitude image of the time series, where the MR-compatible ablation catheter is visible in hypo-intensity inside the sheep LV (yellow arrow). A ROI of 9 × 9 pixels

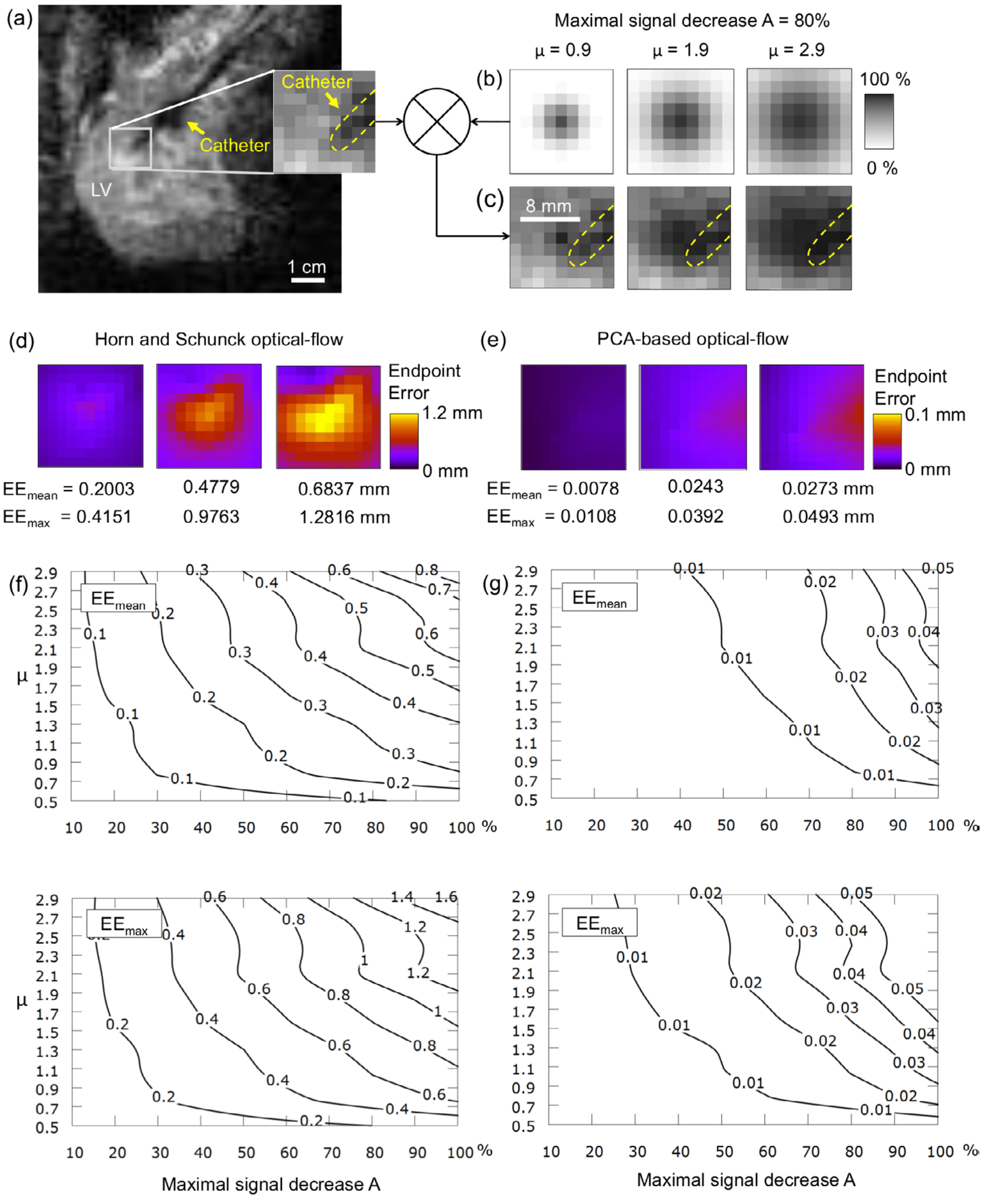

Figure 6. Simulation of a local signal decrease on the magnitude image in sagittal orientation of a sheep LV (a) with a MR-compatible catheter inside (yellow arrow). Several patterns of signal drop were computed depending on the variance μ in pixels and the maximal decrease A in percentage. Example of patterns is shown in (b) with a maximal decrease at the center of the ROI of 80%. Motion estimation was performed on the resulting simulated magnitude images (c). The motion fields EE was computed in millimeters (1 pixel = 1.6 mm) with H&S (d) and PCA-based H&S (e) optical-flow methods (mean and maximal values over the ROI annotated below). Averaged and maximal EE were calculated for each pattern and summed up on contour plots (f) H&S and (g) PCA-based H&S in millimeters.

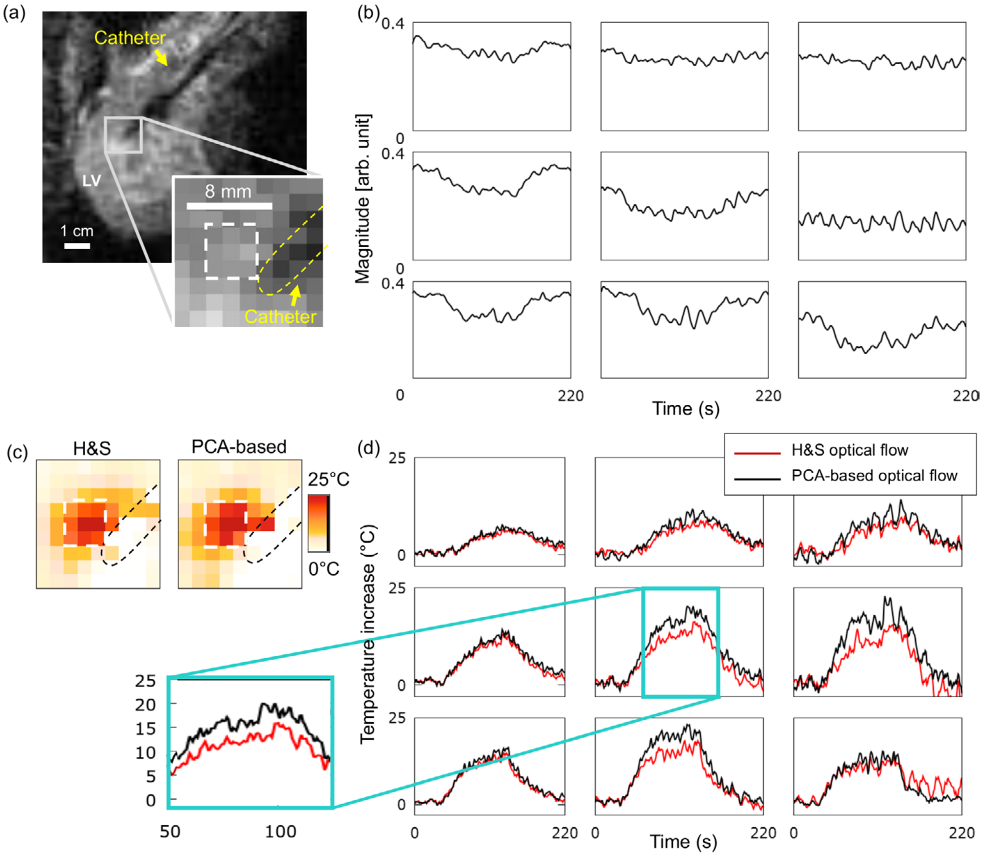

Figure 7. Experimental results of RF ablation under MR temperature imaging *in vivo* in sheep. A RF ablation was run for 60 s at 30 W using a catheter located into the LV. Free-breathing dynamic magnitude images (a) were acquired during RF ablation and used to compensate for respiratory motion. Magnitude signal loss over time in 3 × 3 pixels close to the catheter tip is plotted in (b). Temperature maps (c) were computed using H&S and PCA-based H&S optical-flow algorithms for motion estimation. Temperature evolution in time in 3 × 3 pixels (surrounded by the white dashed box) was plotted in (d) to compare results achieved with both tested methods.

was selected at the distal tip of the catheter for the simulation of several patterns of signal intensity drop. Examples of these patterns are shown in figure 6(b) with a maximal signal decrease A of 80% and various values of variance μ from 0.9 to 2.9 pixels. These patterns were applied to the original magnitude image to simulate a change in myocardial tissue properties with heating (figure 6(c)). Corresponding EE maps were computed with H&S (figure 6(d)) and PCA-based H&S (figure 6(e)) motion estimation method, showing that the misregistration were higher using the H&S algorithm. For example, a signal decrease pattern (A, μ) of (80%, 1.9 pixels) resulted in a maximal EE of ~0.98 mm with the H&S algorithm compared to ~0.04 mm with the PCA-based H&S method. Contour plots displayed in figures 6(f) and (g) confirm that the latter method is more robust in terms of mean and maximal EE values.

To evaluate the impact of motion estimation errors, original experimental data with RF ablation heating on the LV was used to compute the temperature maps using the two different methods for motion estimation. The signal decrease in the pixels around the catheter tip (figure 7(a)) is displayed in figure 7(b). Motion-induced susceptibility artifacts were successfully corrected with both methods and a heating spot is clearly visible near the tip of the catheter, as shown in figure 7(c). However, a difference in temperature elevation (up to 5 °C) was observed in the 3 hottest pixels with the PCA-based H&S algorithm (figure 7(d)). The signal drop in these pixels was about 40% with a variance $\mu = 0.7$ pixel in a limited area in the vicinity of the catheter tip.

4. Discussion

Real-time cardiac thermometry was achieved with a spatial resolution of $1.6 \times 1.6 \times 3\,\text{mm}^3$ and a temporal resolution of ~4–5 slices/heartbeat, as already reported (Ozenne *et al* 2016). However, the accuracy of temperature measurements relies on the efficiency of the motion registration algorithm together with the correction of the susceptibility artifacts. The standard method for motion estimation in the context of MR thermometry on moving organs is the use of optical-flow algorithms that interpret intensity variation on magnitude images as local displacement of the pixels. In this paper, the impact of signal decrease during RF ablation on the motion estimation was quantitatively investigated, and the PCA-based optical-flow algorithm was demonstrated to be more robust against potential local intensity variation on magnitude images during heating.

The required learning step does not increase the duration of the standard MR thermometry procedure since collection of data prior to heating is also necessary for compensating susceptibility artifacts on phase images. Since only a limited number of respiratory cycles is required to collect learning data (typically 20 s scanning were found sufficient to cover two to three respiratory cycles), such a method remains compatible with clinical practice. Moreover, the MR thermometry pipeline is fully automatic and does not require the intervention of an operator (for ROI segmentation for example). The calibration is limited to only two parameters (number of eigenvectors and regularization term α) and can be performed on representative image data-sets. For the tested images in this study, we showed that any value of α in the range of 0.05–0.1 combined with a minimum number of 3 eigenvectors (figure 1) were sufficient to ensure good results. Compared with the conventional H&S optical-flow, the PCA-based technique provided similar results on all volunteers in term of TSD (value around 1 °C in the LV, see figure 2), which is sufficient to accurately measure the temperature evolution during RF ablation that typically results in temperature increase higher than 20 °C in the myocardium.

In this paper, a simulation protocol was presented to quantify the impact of different patterns of signal loss on motion estimation. EE contour plots were computed by comparing the estimated motion on the original image with the motion calculated on images containing signal intensity variations that were not observed during the pre-heating learning step. Results showed that conventional PCA-based H&S optical-flow algorithm was less impacted by local intensity variation with a motion field EE 20-fold lower than with the standard H&S method. The conventional H&S motion fields' error was more significant on the phantom than *in vivo* on sheep LV images: ~2 mm and ~0.8 mm of averaged EE (see figures 3 and 6), respectively. Such a difference can be attributed to the different features of the magnitude images in both situations. The gel phantom image presented a rather uniform disk clearly delineated from the background and only a limited number of pixels were hypointense near the catheter tip. On the contrary, cardiac MR images were noisier, with a much lower number of pixels covering the myocardium on the LV and a larger number of hypointense pixels were visible since the catheter was included into the imaging plane. Therefore, the same simulated patterns may result in different contributions on misregistration using optical flow algorithms.

The impact of misregistration using conventional H&S algorithm was then investigated on experimental data during RF delivery. The resulting temperature error could be computed on a static phantom since the reference temperature could be measured. Conventional H&S was found to sharply impact the calculated temperature map (up to 15 °C of temperature error) while the PCA-based H&S allows for an accurate temperature calculation (below 1.5 °C of temperature error). The motion fields' EE was in good agreement with the prediction of the simulation, considering the fact that experimental intensity change was not as isotropic as simulated one. The simulated signal drop patterns were designed to mimic the aspect of catheter-based RF ablation, but other patterns may be implemented to simulate different heating sources (e.g. Laser, high intensity focused ultrasound, microwave) (Lepetit-Coiffé *et al* 2010).

Comparison of temperature maps obtained with both optical-flow methods was finally performed in presence of motion on a phantom and *in vivo* in sheep LV during RF ablation. As on static phantom, temperature maps were sharply different by only changing the optical-flow algorithm. The temperature increase using PCA-based H&S motion estimation was close to the optical fiber probe located near the catheter tip. The impact of intensity drop on final temperature maps was found larger on the gel phantom (up to 15 °C) than on the sheep LV (up to 5 °C). As mentioned above, the influence of artifact on temperature estimate depends on the image features. Images obtained on the heart of the sheep shows a hyposignal around the catheter. Therefore, relative intensity drops are lower when considering a given area around the catheter, as compared to images acquired on the gel. Further studies may include RF ablation in gels having inclusions of compounds with different signal intensities to simulate various experimental conditions. However, experimental results were consistent with simulated motion fields' EE (see figures 3 and 6) considering the amplitude and the variance of the intensity variation that were smaller *in vivo* than in phantom. Therefore, the methodology presented in this work does not require particular assumptions and may be applied for each particular situation.

In order to be clinically applicable, computation time of the algorithms must be shorter than 100 ms (scan-time per image) to avoid latency in the real-time processing. Using the parameter $\alpha = 0.1$ and five eigenvectors with the PCA-H&S algorithm, computation time was of 25 ms per image, which was approximately 2.5 times shorter than the conventional H&S algorithm (63 ms). Computation time may be shortened by adjusting the regularization parameter α (reducing α increases the motion estimation computation time) whereas the number of eigenvectors has no influence on the computation time. A GPU-based implementation may also allow a significant reduction of the processing time per slice. However it was found sufficiently fast with its current implementation with the frame-rate of the thermometry sequence for monitoring cardiac RF ablation.

The proposed technique is constrained to displacements that can be characterized as a linear combination of the prior learned motion. However, a complete re-calibration may be required in case of significant changes in the motion pattern and/or in the image features, such as the modification of the catheter position than can occur during the RF ablation procedures. Similarly, the use of this method on patients suffering from cardiac arrhythmia need to be evaluated. In presence of arrhythmia, image acquisition can occur at different cardiac phases due to a change in synchronization related to the ECG. Cardiac contraction patterns that have never been observed during the learning step may therefore be difficult to compensate. Adaptive PCA algorithms should be investigated to automatically adapt in real-time without stopping the acquisition and reacquire a new learning data set. Alternatively, artifacted images in the time series may be identified and rejected from the pipeline. For this purpose, an inter-correlation coefficient between each new magnitude image and corresponding reference may be computed online and used as a criterion for rejection to maintain stability of the thermometry, at the cost of the update rate of temperature imaging. Other approaches may include an analysis of the ECG pattern (e.g. mean ± SD of the cardiac cycle duration) during the learning step in order to evaluate the ratio of cardiac cycles exhibiting variations. From this analysis, an optimal trigger delay may be defined to ensure keeping most of the images in the pipeline.

Imaging slices positioned in coronal and sagittal orientations were assumed to fully encompass respiratory motion. However, residual through-plane motion may remain, depending on the patient anatomy and breathing pattern. Integration of an echo-navigator to the thermometry pulse sequence followed by slice repositioning may help to overcome this limitation (Köhler *et al* 2011, de Senneville *et al* 2012).

5. Conclusion

In this paper, the robustness of the PCA-based H&S method was evaluated in the context of tissue MR properties changes during RF ablation in the perspective of cardiac treatment of arrhythmia. This algorithm accurately estimates the heart motion in presence of signal intensity variations due to heating and remains compatible with a frame rate of 10 images per second. The PCA-based H&S algorithm is faster and less sensitive to local variations of signal intensities associated with temperature than conventional H&S algorithm.

Acknowledgement

Authors gratefully acknowledge Viginie Loyer and Delphine Vieillot for assistance in animal care. This work received financial support from the French National Investments for the Future Programs ANR-10-IAHU-04 (IHU Liryc), Laboratory of Excellence ANR-10-LABX-57 (TRAIL) and the research program ANR-11-TecSan-003-01 (TACIT).

References

de Senneville B D, Mougenot C, Quesson B, Dragonu I, Grenier N and Moonen C T W 2007 MR thermometry for monitoring tumor ablation *Eur. Radiol.* **17** 2401–10

de Senneville B D, Roujol S, Jaïs P, Moonen C T W, Herigault G and Quesson B 2012 Feasibility of fast MR-thermometry during cardiac radiofrequency ablation: feasibility of fast MR-thermometry during cardiac RF ablation *NMR Biomed.* **25** 556–62

Denis de Senneville B, El Hamidi A and Moonen C 2015 A direct PCA-based approach for real-time description of physiological organ deformations *IEEE Trans. Med. Imaging* **34** 974–82

Graham S J, Bronskill M J and Henkelman R M 1998 Time and temperature dependence of MR parameters during thermal coagulation of *ex vivo* rabbit muscle *Magn. Reson. Med.* **39** 198–203

Hansen M S and Sørensen T S 2013 Gadgetron: an open source framework for medical image reconstruction: Gadgetron *Magn. Reson. Med.* **69** 1768–76

Holbrook A B, Santos J M, Kaye E, Rieke V and Pauly K B 2010 Real-time MR thermometry for monitoring HIFU ablations of the liver *Magn. Reson. Med.* **63** 365–73

Horn B K and Schunck B G 1981 Determining optical flow *Artif. Intell.* **17** 185–203

Köhler M O, Denis de Senneville B, Quesson B, Moonen C T W and Ries M 2011 Spectrally selective pencil-beam navigator for motion compensation of MR-guided high-intensity focused ultrasound therapy of abdominal organs *Magn. Reson. Med.* **66** 102–11

Lepetit-Coiffé M, Laumonier H, Seror O, Quesson B, Sesay M-B, Moonen C T W, Grenier N and Trillaud H 2010 Real-time monitoring of radiofrequency ablation of liver tumors using thermal-dose calculation by MR temperature imaging: initial results in nine patients, including follow-up *Eur. Radiol.* **20** 193–201

Lipsman N, Schwartz M L, Huang Y, Lee L, Sankar T, Chapman M, Hynynen K and Lozano A M 2013 MR-guided focused ultrasound thalamotomy for essential tremor: a proof-of-concept study *Lancet Neurol.* **12** 462–8

McDannold N, Tempany C M, Fennessy F M, So M J, Rybicki F J, Stewart E A, Jolesz F A and Hynynen K 2006 Uterine leiomyomas: MR imaging–based thermometry and thermal dosimetry during focused ultrasound thermal ablation *Radiology* **240** 263–72

Ozenne V *et al* 2016 Improved cardiac magnetic resonance thermometry and dosimetry for monitoring lesion formation during catheter ablation *Magn. Reson. Med.*

Ramsay E, Mougenot C, Köhler M, Bronskill M, Klotz L, Haider M A and Chopra R 2013 MR thermometry in the human prostate gland at 3.0 T for transurethral ultrasound therapy: prostate MR Thermometry at 3 T *J. Magn. Reson. Imaging* **38** 1564–71

Rickey D W, Picot P A, Christopher D A and Fenster A 1995 A wall-less vessel phantom for Doppler ultrasound studies *Ultrasound Med. Biol.* **21** 1163–76

Roujol S, Ries M, Quesson B, Moonen C and Denis de Senneville B 2010 Real-time MR-thermometry and dosimetry for interventional guidance on abdominal organs *Magn. Reson. Med.* **63** 1080–7

Sapareto S A and Dewey W C 1989 Thermal dose determination in cancer therapy *Int. Contact Lens Clin.* **16** 340–6

Seror O, Lepetit-Coiffé M, Le Bail B, de Senneville B D, Trillaud H, Moonen C and Quesson B 2008 Real time monitoring of radiofrequency ablation based on MR thermometry and thermal dose in the pig liver *in vivo Eur. Radiol.* **18** 408–16

Tanner H, Hindricks G, Volkmer M, Furniss S, KüHlkamp V, Lacroix D, De Chillou C, Almendral J, Caponi D, Kuck K-H and Kottkamp H 2010 Catheter ablation of recurrent scar-related ventricular tachycardia using electroanatomical mapping and irrigated ablation technology: results of the prospective multicenter euro-VT-study *J. Cardiovasc. Electrophysiol.* **21** 47–53

Weerasooriya R *et al* 2011 Catheter ablation for atrial fibrillation *J. Am. Coll. Cardiol.* **57** 160–6

Wittkampf F H and Nakagawa H 2006 RF catheter ablation: lessons on lesions *Pacing Clin. Electrophysiol.* **29** 1285–97